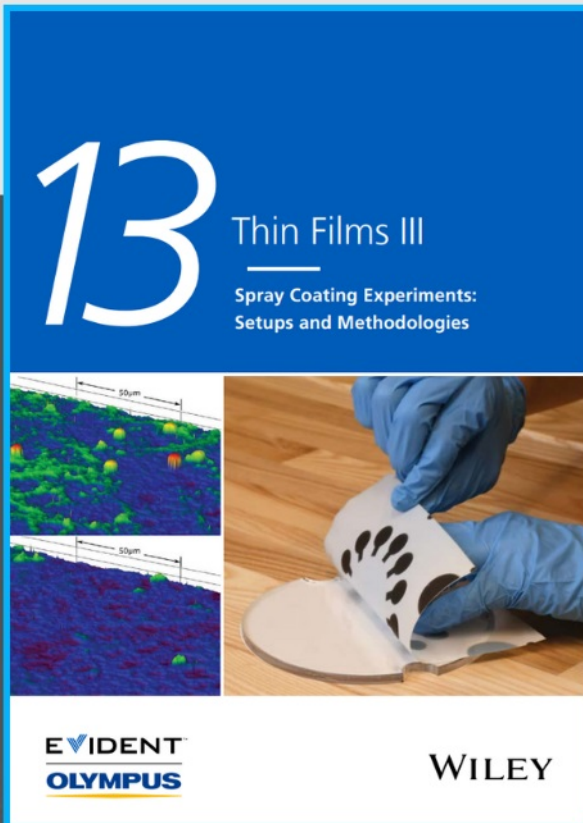# Spray Coating Experiments: Setups and Methodologies

The latest eBook from Advanced Optical Metrology. Download for free.

Spray Coating Experiments: Setups and Methodologies, is the third in our Thin Films eBook series. This publication provides an introduction to spray coating, three article digests from Wiley Online Library and the latest news about Evident's Image of the Year Award 2022.

Wiley in collaboration with Evident, are committed to bridging the gap between fundamental research and industrial applications in the field of optical metrology. We strive to do this by collecting and organizing existing information, making it more accessible and useful for researchers and practitioners alike.

13 Thin Films III

Spray Coating Experiments: Setups and Methodologies

EVIDENT OLYMPUS

WILEY

RESEARCH ARTICLE

A Spiky Silver-Iron Oxide Nanoparticle for Highly Efficient Targeted Photothermal Therapy and Multimodal Imaging of Thrombosis

Karla X. Vazquez-Prada, Shehzahdi S. Moonshi, Yuao Wu, Fahima Akther, Brian W.C. Tse, Kamil A. Sokolowski, Karlheinz Peter, Xiaowei Wang, Gordon Xu, and Hang Thu Ta*

Thrombosis and its complications are responsible for 30% of annual deaths. Limitations of methods for diagnosing and treating thrombosis highlight the need for improvements. Agents that provide simultaneous diagnostic and therapeutic activities (theranostics) are paramount for an accurate diagnosis and rapid treatment. In this study, silver-iron oxide nanoparticles (AgIONPs) are developed for highly efficient targeted photothermal therapy and imaging of thrombosis. Small iron oxide nanoparticles are employed as seeding agents for the generation of a new class of spiky silver nanoparticles with strong absorbance in the near-infrared range. The AgIONPs are biofunctionalized with binding ligands for targeting thrombi. Photoacoustic and fluorescence imaging demonstrate the highly specific binding of AgIONPs to the thrombus when functionalized with a single chain antibody targeting activated platelets. Photothermal thrombolysis in vivo shows an increase in the temperature of thrombi and a full restoration of blood flow for targeted group but not in the non-targeted group. Thrombolysis from targeted groups is significantly improved ($p < 0.0001$) in comparison to the standard thrombolytic used in the clinic. Assays show no apparent side effects of AgIONPs. Altogether, this work suggests that AgIONPs are potential theranostic agents for thrombosis.

1. Introduction

Cardiovascular disease (CVD) is the global leading cause of morbidity.[1] Thrombosis, the formation of potentially deadly blood clots in an artery or vein, contributes to one in every four deaths worldwide.[2] Atherosclerosis with the rupture of unstable plaques, ultimately the formation of thrombi and finally myocardial infarction is the most frequent example on how thrombosis causes a large burden of mortality and morbidity.[3,4] Early diagnosis of thrombosis is crucial for its effective treatment and decreases its recurrence.[5,6] Current treatment and diagnosis of thrombosis have some limitations including the use of radiation, invasiveness, low specificity, substantial economic burden, and side effects such as potentially deadly bleeding.[6–13] Some of the emerging non-invasive imaging techniques for the accurate diagnosis of CVDs include magnetic resonance imaging (MRI) and photoacoustic imaging (PAI).[14,15] The main advantages of MRI and PAI over conventional techniques include higher tissue penetration depth, high spatial resolution, the lack of ionizing radiation, non-invasiveness, and the ability to track treatment progression.[16,17] One of the challenges of MRI and PAI for CVDs is the improvement of the binding specificity of contrast agents, such as iron oxide nanoparticles (IONPs) and metallic nanoparticles.[18,19]

Nanotechnology has become an important tool in biomedicine for the diagnosis and treatment of numerous diseases, including

K. X. Vazquez-Prada, S. S. Moonshi, Y. Wu, F. Akther, H. T. Ta
Queensland Micro- and Nanotechnology
Griffith University
Nathan, Queensland 4111, Australia
E-mail: h.ta@griffith.edu.au

K. X. Vazquez-Prada, F. Akther, G. Xu, H. T. Ta
Australian Institute for Bioengineering and Nanotechnology
the University of Queensland
St Lucia, Queensland 4072, Australia

B. W.C. Tse, K. A. Sokolowski
Translational Research Institute
Woolloongabba, Queensland 4102, Australia

K. Peter, X. Wang
Baker Heart and Diabetes Institute
Melbourne, Victoria 3004, Australia

K. Peter
Department of Medicine
Monash University
27 Rainforest Walk, Clayton, VIC 3800, Australia

H. T. Ta
School of Environment and Science
Griffith University
Nathan, Queensland 4111, Australia

ADVANCED
SCIENCE NEWS
www.advancedsciencenews.com

NANO · MICRO
small
www.small-journal.com

CVDs.[20,21] One of the key advantages of nanomedicine is its ability to generate submicrometric-size agents conveying targeting, diagnostic, and therapeutic moieties.[22–24] Moreover, the combination of diagnostic and therapeutic elements into one single nanoparticle has led to the development of a new concept termed "theranostics".[25] Nanotheranostic agents aim to improve diagnosis, achieve targeted therapy, monitor biodistribution, and response to therapy with increased safety and efficacy.[25–29]

Iron oxide nanoparticles (IONPs) are widely used in biomedical applications due to their surface chemistry, antimicrobial effectiveness, non-toxicity, biocompatibility, and superparamagnetism characteristic.[30–33] IONPs display super magnetism and therefore show promising potential to act as diagnostic tools for MRI.[34–38] IONPs can also be a therapeutic tool as they can act as colloidal mediators for cancer treatment using magnetic hyperthermia and as drug delivery systems.[39–43] IONPs coated with metals like gold have been shown to display negative contrast for MRI and near-infrared (NIR) localized surface plasmon resonance (SPR) (700–850 nm).[44] Recently, we reported the synthesis of silver-iron oxide nanoparticles with SPR tuned at NIR range for imaging and therapeutic applications.[45] SPR occurs when an incident light penetrates a material and polarizes the conduction of electrons, causing an increase in temperature.[46] Tuning the shape of the nanoparticles might be one approach for shifting the absorbance peak of the material to this region, where soft tissue, haemoglobin, and water absorb weakly.[47] Elongating a spherical nanoparticle into a rod-like shape or nanorose tends to shift the SPR into the NIR. Asymmetrical shapes have lower energy compared to symmetric nano-heaters of equal volume and generate higher temperatures.[48,49] Nanomaterials with strong absorbance in the NIR can be efficient and stable nanoplatforms for imaging and treatment of CVDs with PAI and photothermal therapy (PTT), respectively. NIR PTT involves ablation of the thrombi when exposed to an external optical stimulus, such as a NIR laser.[50] Gold, copper, and silver are elements known as photothermal ablators. Silver nanoparticles have the highest efficiency of plasmon excitation in the visible spectrum[43,48,51,52] and are also known to be effective PAI contrast agents.[41,53,54] When the tissue is illuminated with light pulses, their rapid absorption by PA contrast agents enables photons to generate ultrasound waves and heat, permitting simultaneous PAI and PTT.[55]

In this study, we attempted to develop silver-iron oxide nanoparticles (AgIONPs) for highly efficient targeted photothermal therapy and imaging of thrombosis. Small iron oxide nanoparticles were employed as seeding agents for the generation of the spiky AgIONPs with strong absorbance in the NIR range, which is reported herein for the first time in the literature. This research not only develops a nanoparticle system with strong NIR and PAI responses, but also potentiates a new generation of nanotheranostic agents for the less invasive and specific targeted treatment of thrombosis.

2. Experimental Section

An extended and exhaustive version of the materials and the methodology used in this research can be found in the Supporting Information section.

2.1. Optimization of the Silver Nanorose Growth on Citrate-IONPs (AgIONPs)

Silver coating on the surface of IONPs was conducted following the protocol of Ma et al.[44] with slight modifications. Optimization of the silver coating was obtained by varying the quantity, addition rate, the metal cation molar ratio, and the reaction time. The optimized protocol consisted of IONPs made in an aqueous solution made with 0.144 mg of iron. Hydroxylamine 50% (20 µL) and trisodium citrate (TSC) (70 µL of 1.14%) were added into the solution under continuous stirring and served as a seeding agent for the elemental silver. Aliquots of $AgNO_3$ (6.348 mM) were added to the solution every 10 min until the amount of $AgNO_3$ added was 250 µL (50 µL per aliquot). Vigorous stirring (600 rpm) was carried throughout the whole synthesis. An additional 75 µL of TSC (1.14%) was added at the end of the synthesis to stabilize the nanoparticles. The densely AgIONPs were separated from the less densely uncoated IONPs by centrifugation at 4000 g for 6 min and redispersed in deionized water. Dialysis overnight with 5 mL of water helped on the purification of the nanoparticles (AgIONPs). AgIONPs were then coated with a polymer to increase stability and biofunctionalized with different ligands targeting thrombi (Supporting Information).

2.2. Characterization of the Nanoparticles

Dynamic light scattering (DLS) in a Zetasizer Nano ZS (Malvern) was used to obtain the average hydrodynamic size and the size distribution of AgIONPs. Transmission Electron Microscopy (TEM) images and Energy Dispersive X-ray Spectroscopy (EDS) were taken on a JEOL-JEM-1010 Transmission Electron Microscope. The absorption of the nanoparticles was determined using a CARY 60 UV–vis spectrophotometer (200–1000 nm). The amounts of all the metals were determined by inductively coupled plasma-optical emission spectroscopy (ICP-OES) (Optima 8300DV ICP-OES from Perkin Elmer). The transverse relaxivity of the nanoparticles was measured with a Bruker 9.4T MRI scanner.

MRI phantom vessels containing different concentrations of AgIONPs (100 µL) were prepared. Concentration of iron was quantified by ICP-OES. MRI of phantoms was performed using a 9.4T MRI scanner (Bruker). T_2-weighted images were acquired using the following parameters: repetition-time (TR) = 2,600 ms, echo-time (TE) = 7–896 ms, field of view (FOV) = 58 mm x 58 mm, matrix-size = 256 × 256, slice thickness = 1 mm, and bandwidth = 50 kHz. PAI was carried out using a Vevo LAZR scanner (Visualsonics, Toronto, Canada) as discussed in previous reports.[56] Different concentrations of AgIONPs samples were loaded into polyethylene tubes. The PA spectral signature of AgIONPs was determined by scanning from 680 to 970, with 5 nm increments, and analyzed using the Vevolab 5.6.1 software. The PA profile was validated by a 3D scan covering 10 mm along the length of tubing with excitation at 808 nm.

Human fresh frozen plasma (FFP) provided by the Australian Red Cross Service was added (180 µL) to an Eppendorf tube. A mixture of 5 µL of $CaCl_2$ (1 M), 12 µL of actin, and 3 µL of thrombin (0.1 U µL^{-1}) was added to the FFP. The mixture

was incubated for 1 h at 37 °C. After incubation, the clots were washed with PBS 7.4 at room temperature with subtle rotation for 30 min. Before incubation, it was confirmed that all the ligand-conjugated nanoparticles used in this assay had the same fluorescence intensity. The tested nanomaterials were resuspended in PBS 7.4. A concentration of nanomaterials at 0.1 mg mL^{-1} was used for fluorescence imaging and 0.4 mg mL^{-1} for photoacoustic imaging. The clots were incubated with solution under rotation for 15 min following by three washes with PBS of 15 min each. The clots were fixed with 4% paraformaldehyde (PFA) and imaged using a Sapphire machine on fluorescence mode (scanning with all fluorescence filters). For PAI scanning, clots were immersed in a bed of ultrasound gel, then imaged with excitation at 780 nm, gain of 30 dB, step size of 0.1 mm, covering the length of the clots.

An in-house polydimethylsiloxane (PDMS) multichannel microfluidic device was used to check the binding affinity of the nanoparticles under flow (see method in Supporting Information).[57]

2.3. In Vitro Thrombolysis Assay

In vitro human thrombi were prepared from blood provided by the Australian Red Cross under a human ethics (2021/598) approved by Griffith University human ethics committee. Briefly, the blood was centrifuged for 15 min at 250 g. The pellet (Red blood cells; RBC) and the supernatant (platelet-rich plasma; PRP) were collected. A solution of 95% FFP and 5% RBC was made in order to mimic the composition of human arterial thrombi.[58] For preparing each thrombus, 200 µL of this mixture was added to 5 µL of 1 M CaCl$_2$ in a glass vial. The mixture was incubated for 15 min at room temperature. The glass vials were weighed before and after the experiment. The initial and final temperature were also recorded with a thermal camera (FLIR, US). Thrombi were incubated with 100 µL of different concentrations of the nanoparticles and optimization of the settings was made. PBS was used as the control in all the thrombolysis experiments. The thrombi were irradiated with an 808 nm infrared laser (light intensity = 1, 1.5, and 2 W cm^{-2}, laser-diameter = 2 cm) for 1, 2, and 3 min in a custom build stabilized infrared fiber laser system. After the laser exposure, the liquid of the lysis was discarded and the decrease in the clot's mass was calculated for each thrombus. The percentage decrease in the thrombus mass was normalized against that of the control.

2.4. In Vivo Photoacoustic and Fluorescence Imaging

All animal procedures were performed in accordance with the Guidelines for Care and Use of Laboratory Animals of the University of Queensland. Approval number: No. AIBN/420/19/CAI and 2020/AE000350.

Two different groups of mice were analyzed for imaging purposes, including targeted (scFv-PEG@AgIOPs) and non-targeted (mut-scFv-PEG@AgIONPs) delivery. All mice were first imaged by color Doppler around the neck region to identify the precise location of the artery, then imaged for photoacoustic signals at pre-injection, 10, 20, and 30 mins post-injection. Mice

received an intravenous injection of AgIONPs at 4 mg kg^{-1} of body weight. 3D PA scans were performed at the excitation of 780 nm, frame averaging of 2, covering 10 mm along the length of the artery at 0.1 mm step size, and respiration gating activated. All analyses including PA signal intensity measurements and visualizations were performed using Vevolab software v5.6.1 with 30 dB gain.

Fluorescence imaging (FI) was obtained using the IVIS Spectrum Perkin Elmer). Mice were anaesthetized with 1–2% isoflurane at oxygen flow of 1–2 L min^{-1}. FI was performed at the emission and excitation of 640 and 790 nm, respectively. Images were taken at pre-injection, 5, 10, 15, 20, 25, and 30 min. Fluorescence intensity and total radiant efficiency were calculated using the IVIS software v4.5.

2.5. In Vivo Thrombolysis

Five groups of mice were used for this study, including PBS group, non-targeted group, targeted group, and tPA group. Blood flow was measured before the induction of thrombus, immediately after the induction, and after laser treatment with a 0.5 mm flowmeter probe (Transonic) at 160 Hz. For targeted and non-targeted groups, AgIONPs were injected at a dose of 4 mg kg^{-1}. Group treated with tissue plasminogen activator (tPA) were injected at a dose of 2 mg kg^{-1}. The clot area was irradiated by the 808 nm laser at 1 W cm^{-2} for 3 min and rested for 5 min prior to the next laser exposure for total three exposures. All laser experiments were performed after 1 h of thrombus induction. The temperature before and after laser irradiation was obtained using infrared thermal camera (FLIR C2) in every cycle. The change in the maximum and minimum flow value was calculated between the five groups. The carotid artery was collected before euthanasia, washed with PBS, imaged and fixed with 4% PFA. The collected carotid artery was then processed and embedded cryosections (5 µm) were further stained with Masson's trichrome. The prepared histological slides were observed under the microscope (Olympus Upright FL Microscope BX63) and analyzed for thrombus area with ImageJ.

2.6. Statistical Analyses

One-way and two-way ANOVA were performed using the software GraphPad Prism, at confidence levels of 95% and 99%, and using Bonferroni or Tukey post-hoc tests. Assays were at least made in triplicates. For in vivo experiments, the sample size was at least $n = 4$. All graphs were plotted using GraphPad Prism 9, with *$p < 0.05$ considered significant while **$p < 0.01$, ***$p < 0.001$, and ****$p < 0.0001$ to be very significant. Results are presented as mean ± SD.

3. Results and Discussion

3.1. Physicochemical Features of IONPs and AgIONPs

Following design and optimization, IONPs were successfully synthesized (Figure S1, Supporting Information) with the

ADVANCED
SCIENCE NEWS
www.advancedsciencenews.com

NANO · MICRO
small
www.small-journal.com

co-precipitation of Fe (II) and Fe (III) chlorides in an alkaline solution at 70 °C. DLS data show that the nanoparticles had a homogeneous distribution with a PDI of 0.16 ± 0.01. The Z-average and number mean particle size were 29.5 ± 0.2 and 16.9 ± 0.5 nm, respectively. The IONPs were effectively coated by citrate, they did not show aggregation and had a negative surface charge (zeta potential = −34.7 mV). TEM images of the nanoparticles confirm the homogeneity in their size and asymmetrical morphology (Figure S1C, Supporting Information).

The silver shell was developed by a seeding method. Based on previous evidence in the literature,[59–61] we know using reducing agents reduce the silver salts from silver nitrate in the solution. For the synthesis of AgIONPs, there were three elements that allowed us to form the seedings for silver nucleation: sodium citrate, hydroxylamine, and the citrate-capped iron oxide nanoparticles. The addition of silver nitrate aliquots formed a silver seeding on the surface of the IONPs. Zhou et al. showed that silver coating on the surface of an oxide was possible due to electrostatic interactions between the surface of the oxide (i.e., graphene oxide) and the silver ions.[62] In our study, the coating of silver on the surface of citrate coated iron oxide nanoparticles is also possible due to the negative surface charge of the citrate coated IONPs. IONPs not only served as a surface template for the silver ion coating, but also as the donor of electrons for the growth of the Ag layer. Moreover, there has been evidence from metal oxide species serving as reducing agent for metal growth on the surface of substrates.[63] Studies show that the physicochemical properties of silver nanoparticles are extremely dependent on the reducing agent used. When silver is reduced by citrate and hydroxylamine, the coating results in an asymmetrical shape due to the presence of small aggregates of silver nanoparticles formed as a consequence of high negative electric charge in the surface. Moreover, the growth of silver (nucleation process) is an autocatalytic reaction.[64,65] The layer of silver on the surface itself is a reactant- more nucleation will occur as more silver is deposited on the surface of the existing layer, promoting the formation of aggregates that provide the AgIONPs their spiky shape and therefore, a higher plasmon resonance and strong absorbance in the NIR.

The hydroxylamine is adsorbed on the IONPs (Fe_3O_4) surface and therefore serves as a reducing agent that favors the formation of elemental silver (Figure S3, Supporting Information). The addition of more reducing agents will generate more seeds and thicken the existing seeds. The AgIONPs silver shell has a strong resonance absorption that can be controlled and shifted to different wavelengths. Our results show that the silver shell was compact and create a near-spherical shape, which had the maximum absorbance peak ≈600 nm. The shape of the nanoparticles became asymmetrical, and the maximum absorbance peak was shifted to the NIR upon increasing the amount of silver or adding more of the reducing agent (Figure S2 and Table S2, Supporting Information). The mass ratio between silver and iron (Ag/Fe) in the reaction, along with the amount of hydroxylamine used, were found as the principal factors of determining the morphology of the nanoparticles and their absorbance (Figure S4 and Table S3, Supporting Information). When the reaction was made with 14 µL of hydroxylamine and a Ag/Fe mass ratio of 0.78 (Figure S4A, Supporting Information) the nanoparticle had a spherical shape. In contrast, when

the IONPs were coated with a ratio of 0.95 and using 20 µL of hydroxylamine, the shape became irregular (Figure S4B, Supporting Information). Moreover, when the reaction occurred with 20 µL of 50% hydroxylamine and at a ratio of 1.18, the spiky shape became more evident (Figure S4C, Supporting Information).

The optimized protocol based on Ag/Fe ratio and amount of hydroxylamine for synthesis of AgIONPs is shown in Figure S4C (Supporting Information). The protocol including addition of 0.171 mg of silver to the IONPs (0.144 mg of iron) with 20 µL of 50% hydroxylamine. Silver nitrate (6.348 mM) was added in five aliquots of 50 µL with a 10 min interval. The optimal protocol was chosen based on the high absorbance at 808 nm which will translate into a higher photothermal efficiency. Using the optimized protocol, the particle diameter increased to 113.4 nm (**Figure** 1B). The particle size distribution seems homogeneous, with a polydispersity index of 0.174 and a negative charge surface (zeta potential = −29.8 mV) (Figure 1B,C). TEM images confirm an asymmetrical shape and low polydispersity (Figure 1A) and UV–vis spectra show a clear maximum absorbance peak in the NIR (Figure 1D). EDS and ICP data show both Fe and Ag in the AgIONPs sample (Figure 1E; Table S3, Supporting Information) while Ag was not detected in the citrate-IONPs. EDS results estimated the iron in the nanoparticles to be 24.34% whereas ICP data show the iron content to be ≈1.2%.

The difference in the measurements could be attributed to the shape and the composition of the nanoparticles. It is known that EDS analyses depend greatly on the sample's surface, homogeneity, and density.[66] The spiky shape of AgIONPs might have caused difficulties to obtain an analytical accuracy, as the X-rays might not have been able to penetrate adequately into the core of the nanoparticle. In addition, the standard used for iron herein had differences in the structure and composition to that of the iron oxide in the AgIONPs, affecting the accuracy of the results.

Moreover, the extinction coefficient of the nanoparticle at 808 nm was estimated to be $\varepsilon = 5.39 \times 10^{12}$ M^{-1} cm^{-1} (Table S1, Supporting Information) suggesting AgIONPs could induce an efficient photothermal effect when exposed to NIR. Compared to other silver nanoparticles in the literature,[67] AgIONPs have up to 34 times higher extinction coefficient. AgIONPs possess significantly higher extinction coefficient at 808 nm when compared to other nanoparticles used for NIR photothermal therapy (up to 83968x).[68–70] The 808 nm laser heat conversion efficiency (η) of the AgIONPs was determined to be 23% (Figure S5, Supporting Information, page 3–4), which is similar or greater to other nanomaterials described in the literature for photothermal therapy, including gold nanorods (≈21.0%, 800 nm laser),[71] Cu_{2-x} Se nanocrystals (≈22%, 800 nm laser),[72] and ICG encapsulated polymeric nanoparticles (≈20.81%, 808 nm laser).[73]

3.2. AgIONP as a Multimodal Imaging Agent

The efficacy of AgIONPs as a bimodal contrast agent was tested by using two non-invasive methods, i.e., PAI and MRI.[74] To examine the effect of particle sizes on the MRI contrast
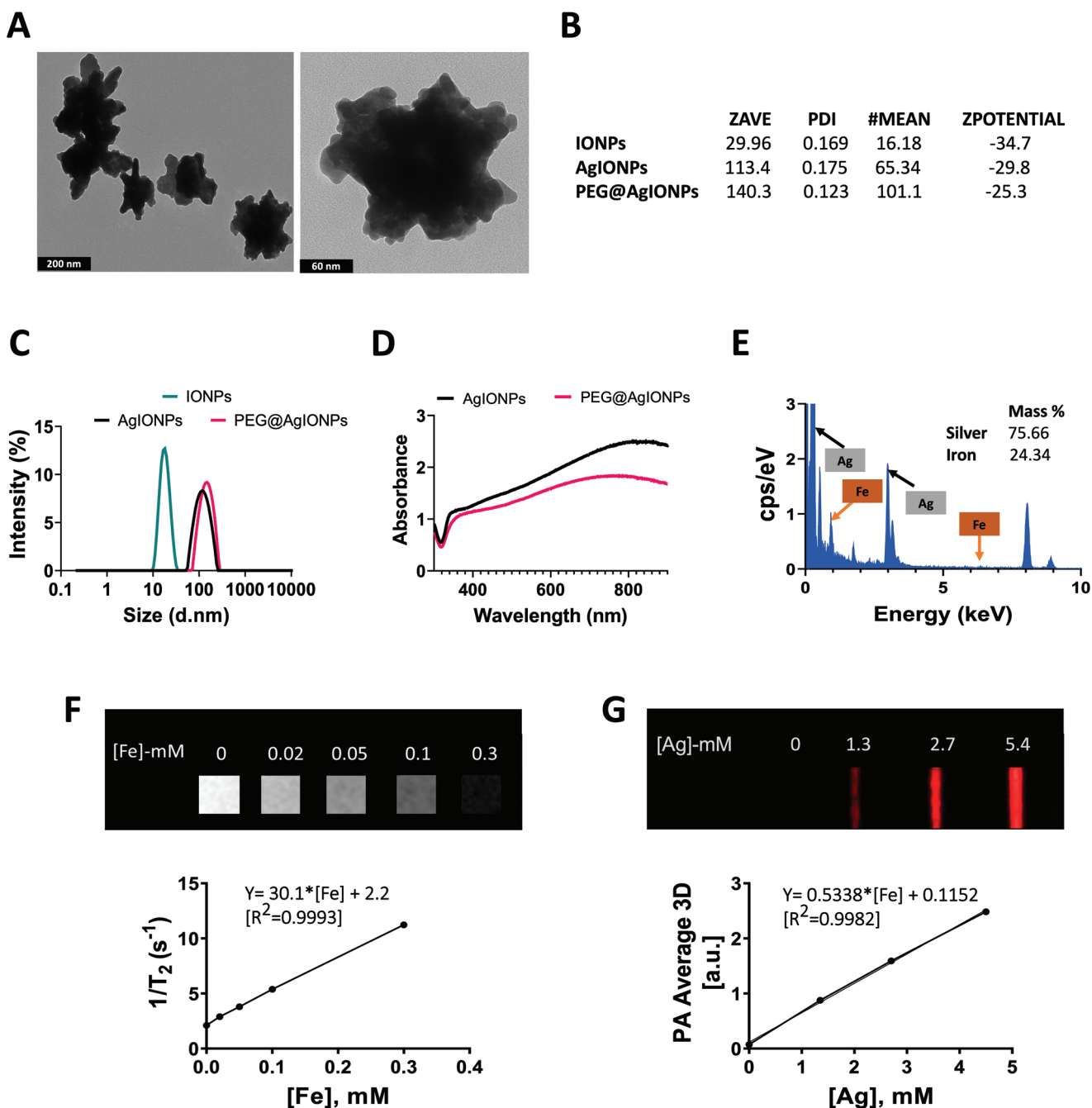
Figure 1. Characterization of the nanosystem. A) TEM images showing AgIONPs with irregular nanorose-like shape. B) Table summary of the parameters from each particle that conforms the nanosystem, C) dynamic light scattering (DLS), and D) absorbance of the nanoparticles. Absorbance of AgIONPs shows an intense peak at 808 nm. E) EDS spectra also illustrates the percentage of silver and iron in an AgIONP. F) MR T_2-weighted images of phantom tubes with AgIONPs showing an enhancement in the contrast signal with each increasing concentration. G) PA images of polyethylene tubes with increasing concentration of AgIONPs.

properties of AgIONPs, the relaxation time of the nanoparticles was studied on a 9.4T MR Scanner. It is known that IONPs can generate a change in the local magnetic field, the resonance properties of a tissue and hence its relaxation time T_2 values. By changing the proton density of a tissue and altering the relaxation properties of surrounding protons, IONPs can serve as a promising contrast agent for MRI. Figure 1F shows the T_2-weighted MRI images of AgIONPs at different concentrations. The T_2-weighted relaxivity (r_2) of the nanoparticles was measured to be 30.1 mM^{-1} s^{-1}. The phantom tubes containing higher concentrations of AgIONPs appeared darker than that containing lower concentrations of AgIONPs. Our nanoparticles appeared to have lower r_2 when compared to IONPs reported in the literature.[74] Interestingly, we found that the r_2 from AgIONPs shown

**ADVANCED
SCIENCE NEWS**

www.advancedsciencenews.com

NANO · MICRO

small

www.small-journal.com

in Figure S4A,B (Supporting Information) was smaller than that in Figure S4C (Supporting Information). It is probable that the more spiky the shape of the nanoparticles, the stronger the MRI effect. In addition, r_2 decreased as the silver layer grew thicker, which explains that our r_2 values were smaller than non-metallic coated IONPs reported in the literature.

PAI is a highly sensitive and new imaging method that measures the heat response in a tissue to laser pulses. Figure 1G shows an increase of signal nanoparticles in a concentration-dependent manner in the PA images of polyethylene tubes containing different concentrations of the. When the nanoparticles interact with light, the conduction of silver electrons is driven by the incident electric field into collective oscillations of localized SPR.

Therefore, the contrast is stronger when the concentration of silver increases due to more free charges on the surface of the AgIONPs that oscillate with the electromagnetic field. Ex vivo data in white male mouse cadaver show that endogenous PA signals derived from blood differed from that of the AgIONPs (Figure S6, Supporting Information). In addition, the figure shows an image comparing the signals from blood tubes and AgIONPs alone, suggesting that the photoacoustic signals are purely provided by the nanoparticles but not any endogenous component. PEGylation of AgIONPs increased the particle size and led to changes of physicochemical properties. The absorbance peak did not change; however, the intensity slightly decreased probably because the soft coating causes the crests of silver to be less exposed to the surface (Figure 1C,D). As expected, the surface charge of the PEG-coated and the uncoated AgIONPs was not significantly different since carboxylated PEG has negative charge. Previous reports in the literature suggest that the surface itself likely consists of a monolayer of Ag^+.[75] Some of the SH-PEG-COOH and SH-mPEG may exist as a thiolate anion and bind with silver ions, which may reduce the absorbance.

The stability assays show that the size and absorbance of naked AgIONPs changed immediately after mixing with PBS. On the contrary, the size of PEG@AgIONPs remained stable for 24 h. The absorbance profile of PEG@AgIONPs did not change compared to non-coated NPs, further suggesting successful PEGylation (Figure S7, Supporting Information).

3.3. In Vitro Thrombolysis Efficacy of AgIONPs

The in vitro thrombolysis assays suggest that the nanoparticles were able to lyse thrombi when exposed to 808 nm laser (**Figure 2**). The optimized settings for thrombolysis using AgIONPs included a nanoparticle concentration of 0.1 mg mL^{-1}, the laser intensity of 1.5 W cm^{-2} for 2.5 min and 3 cycles. The nanoparticles were able to transform light energy from the laser into heat and therefore promoted thrombolysis in a dose dependent way.

Our results are similar to the first generation of AgIONPs developed by us (Rehman et al. paper).[45] Nonetheless, the percentage decrease of thrombus weight was higher in our study (≈1.5x) even when using the same concentration (0.1 mg mL^{-1}) and lower laser intensity. The main reasons for these differences are likely related to the morphology of the nanoparticles.

The AgIONPs from Rehman et al. are nanorose shaped but with less prominent peaks than the nanoparticles synthesized in this study. Importantly, the temperature did not significantly change from cycle to cycle, which is similar to report by Rehman et al. These results suggest that it is possible to enhance the photothermal ablation of thrombi by increasing the number of cycles without compromising surrounding tissue to burns.

3.4. Biofunctionalization of the Nanoparticles Enhanced the Binding Efficiency to Human Thrombi In Vitro

The nanoparticles were targeted to major components of thrombi: fibrin and activated platelets. FibPeps target fibrin whereas RGD peptide and single chain antibody (scFv) bind specifically to activated form of the integrins $\alpha v\beta 3$ and GPIIb/IIIa in platelets, respectively.

3.4.1. Fibrin-Binding Peptide (FibPeps)

The conjugation of the FibPeps was achieved via three independent reactions (Figure S8, Supporting Information). The first reaction consisted of the addition of TCEP. The polymer has thiol groups exposed and might create disulfide bonds between them. The TCEP was added as a reducing agent to break the disulfide bond to free the thiol groups for conjugating AEM to the peptides. Maleimide readily reacts with the thiol groups in the peptides, which favors the conjugation. The second reaction consists in activating the carboxylic groups provided by SH-PEG-COOH on the surface of AgIONPs. Last, we mix both reactions to allow the activated carboxylic groups in the PEG@AgIONPs react with the terminal amine of the peptide.

The conjugation yields of all the protocols assessed are summarized in Table S4 (Supporting Information). When using 4.56 nmoles of the peptide (1:74 mass ratio of FibPeps:NP), the conjugation yield was 27%, which is smaller than when using 2.28 nmoles (1:148 mass ratio FibPeps:NP, 69% conjugation yield). The nanoparticles had a decreased absorbance, suggesting the nanoparticles obtained from 4.56 nmoles were not as stable as those with the other 2.28 nmoles protocol. This can be explained because with increasing the amount of peptide, the amount of TCEP and AEM increases as well. TCEP is prepared and used as a hydrochloride salt (TCEP-HCl). Increasing the amount of TCEP will also change the pH of the reaction, affecting the stability of the nanosystem. Despite the low conjugation yield, similar amounts of peptides/nanoparticle were obtained in with 2.28 and 4.56 nmoles of peptide in the reaction. The optimized protocol resulted in 69% conjugation yield using 2.28 nmoles of peptide, and the prepared nanoparticles showed more intense fluorescence intensity in the binding assays (Figure S12, Supporting Information).

3.4.2. Activated Platelet-Targeted Peptide (RGD)

RGD-AgIONPs were synthesized by carbodiimide mediated reactions between COOH on the surface of PEG@AgIONPs
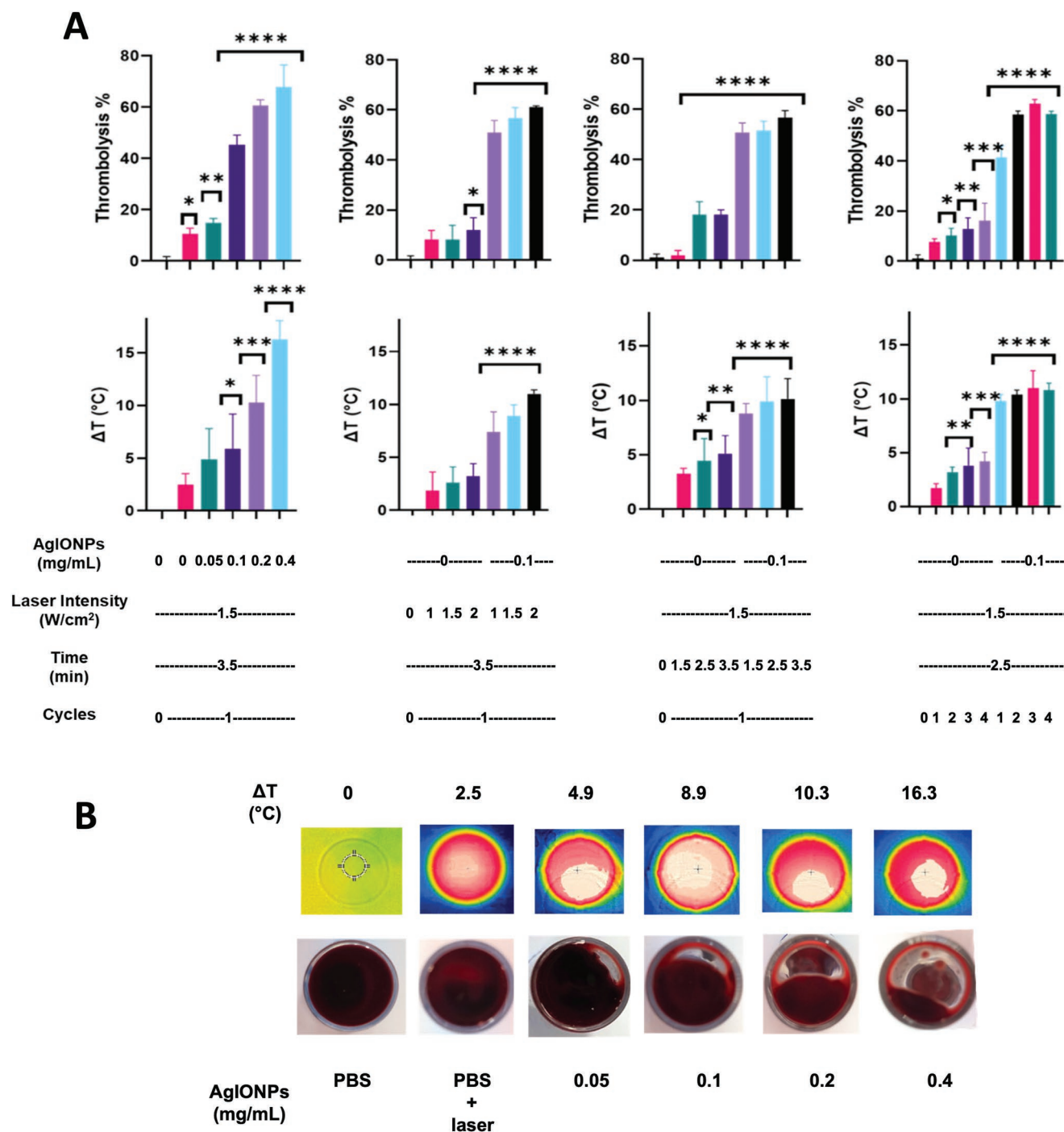
Figure 2. In vitro thrombolysis assay. A) Optimization of the protocol. AgIONPs were able to transform light energy into heat and B) promoted thrombolysis when exposed to 808 nm laser. Thermal images showing heat and the lysis of clot with each concentration ($n = 3$) with $^*p < 0.05$ considered significant while $^{**}p < 0.01$, $^{***}p < 0.001$, and $^{****}p < 0.0001$.

and NH_2 present on Cy5 and RGD (Figure S9, Supporting Information). The optimization of the conjugation to RGD is shown in Table S4 (Supporting Information). The mass ratio of 1:20 (RGD:AgIONPs) was chosen as the optimized protocol since both, the fluorescence and microscope images showed more binding of the nanoparticles to thrombi (Figure S12, Supporting Information). The amount of peptides conjugated onto

nanoparticles increased with adding more peptide to the reaction, while the conjugation yield of RGD to PEG@AgIONPs decreased. Importantly, data showed that RGD-AgIONPs made at 1:20 had the higher binding to thrombi, statistically higher than that at 1:10 and 1:40 (Figure S12, Supporting Information). This could be because the threshold of integrins used for binding was already reached at 1:20 and the addition of more

ADVANCED
SCIENCE NEWS

www.advancedsciencenews.com

NANO · MICRO

small

www.small-journal.com

RGD molecules in DMSO at the higher ratio (1:10) could compromise the stability of RGD-AgIONPs.

3.4.3. Single Chain Antibody (scFv)

Conjugation of a GGG-N$_3$ peptide to the C terminus of scFv-LPETG antibody was achieved via sortase mediated ligation (SML) (Figure S10, step 1, Supporting Information). Successful conjugation of the azide group to the scFv (targeting antibody) and mut-scFv (mutated non-targeting antibody) was indicated by the decrease in size of the resulting conjugated scFv-N$_3$ and mut-scFv-N$_3$ confirmed by SDS-PAGE gel (Figure S11A, Supporting Information). The change in size is due to the loss of LPETG tag during the sortase reaction and has also been reported previously.[35,76] In a separate reaction, the PEG@AgIONPs were modified with Cy5 for fluorescence purposes, and DBCO for copper-free click chemistry reaction with the N$_3$ present on the scFv. The reaction was facilitated by EDC and carbodiimide mediated reaction between COOH on the surface of PEG@AgIONPs and NH$_2$ present on Cy5 and DBCO (Figure S10, step 2, Supporting Information). Labeling of PEG@AgIONPs with Cy5 was further confirmed by the fluorescence intensity measured with Sapphire imager system.

After ligation of the azide group to the antibody and conjugation of Cy5 and DBCO to the nanoparticles, scFv-N$_3$ was reacted with the DBCO-AgIONPs through strain-promoted alkyne-azide cycloaddition (SPAAC). This method allows site specific conjugation of scFv on the surface of the AgIONPs and therefore preserves the antibody binding capacity.[77] SDS-PAGE and BCA assay confirmed conjugation of the scFv and mut-scFv to the nanoparticles. In the SDS-PAGE, indirect measurement of conjugation yield was estimated by loading the supernatant (Figure S11B, Supporting Information ; lane 3&4 for scFv and 6&7 for Mut). Direct measurement was also estimated by loading the whole ScFv-AgIONPs (Figure S11B, Supporting Information ; lane 9) and mut-AgIONPs (Figure S11B, Supporting Information ; lane 8) immediately after the conjugation reaction. As the nanoparticles could not move across the gel, only free (non-bound) antibody molecules moved. The indirect method estimated a conjugation yield of 73.62% for scFv-AgIONPs and of 64.7% for mut-AgIONPs, while the direct method suggested a conjugation of 83.6% and 74.3%, respectively. The percentage shown on Figure S9B (Supporting Information) are the percentage of total antibody molecules moved across the gel.

3.4.4. Comparison of FibPeps, RGD, and scFv-SCE5 Targeted AgIONPs Binding Efficiency to Thrombus

The adhesion of the targeted nanoparticles to human clot was first analyzed in vitro using fluorescence and photoacoustic imaging. All the nanoparticles were tagged with a fluorescent dye. The fluorescence of the incubating solution of each targeted nanoparticle was measured before the assay. Fluorescence imaging was performed to determine which of the targeted nanoparticles would be the optimum for future in

vivo work. There was no difference between the fluorescence intensity of AgIONPs and FibPeps-AgIONPs due to the small amount of peptides per nanoparticle (Figure S12, Supporting Information). Binding of RGD-AgIONPs and scFv-AgIONPs to clot was significantly different ($p < 0.0001$) from that of the control (PBS 7.4) (**Figure 3**A,D). Between these two treatment groups, scFv-AgIONPs had 2x more fluorescence intensity than RGD-AgIONPs. Photoacoustic imaging confirmed the specific binding of scFv-AgIONPs in comparison to mut-AgIONPs (Figure 3B,E).

Flow binding assays further support these findings by showing a significant increase in the binding of Cy5 labeled scFv-AgIONPs to thrombi when compared to mut-AgIONPs. These results are also consistent under simulated artery conditions (Figure 3C,F). The flow conditions of the device and the assay were designed to mimic the pulsatile flow physiology found in arteries with athero-related pathologies (shear rate of 1,000 s^{-1}).[78] The merge between FITC and Cy5 images suggest that there is a specific binding from the targeted nanoparticles to the activated platelets. Moreover, an increase in the intensity of Cy5 signal at different time points suggests that the binding to the thrombus increased gradually over time (Figure S13, Supporting Information). The data gathered in these experiments are a promising sign toward continuing further in vivo studies, as there is not only specific binding from the nanoparticles to the thrombi, but also the binding is maintained under atherothrombosis conditions under physiological flow. One of the advantages of antibodies over peptides is their higher specific recognition and interaction with their epitopes through multiple bonds, and the possibility to target other distinct cellular processes by changing the antibody used. In contrast, the key advantage of peptides over antibodies is their size; being smaller enables them to have good tissue penetration.[79] In our study, we used a single chain antibody, which combines the high affinity of antibodies with smaller molecular size, enabling scFv to have a greater binding efficacy than RGD even with less molecules attached to the AgIONPs. As scFv showed the best binding affinity to thrombus, it was employed for in vivo studies.

3.5. Biocompatibility of PEG@AgIONPs

Hemocompatibility and viability assays were performed to assess the biocompatibility of the nanoparticles. Hemocompatibility was measured photometrically by calculating the hemolysis percentage in the presence of particles assessed by the release of hemoglobin. In our study, PEG@AgIONPs seem to have good hemocompatibility with erythrocytes. The hemolysis percentage was <4% in all the tested concentrations and time periods (**Figure 4**A,B). To test the cytotoxicity of the nanoparticles, Chinese Hamster Ovarian (CHO) cells were incubated with different concentrations of PEG@AgIONPs ranging from 0 to 0.4 mg mL^{-1} of Ag for 24 and 48 h (Figure 4D). Cell viability was assessed by using PrestoBlue Cell Viability Reagent. The cells showed good viability at all tested concentrations. A reduction of cell viability was observed on cells incubated with 0.4 mg mL^{-1} at 48 h. It is important to note that the concentration used in vivo was four times less (0.1 mg mL^{-1}), and

ADVANCED
SCIENCE NEWS
www.advancedsciencenews.com

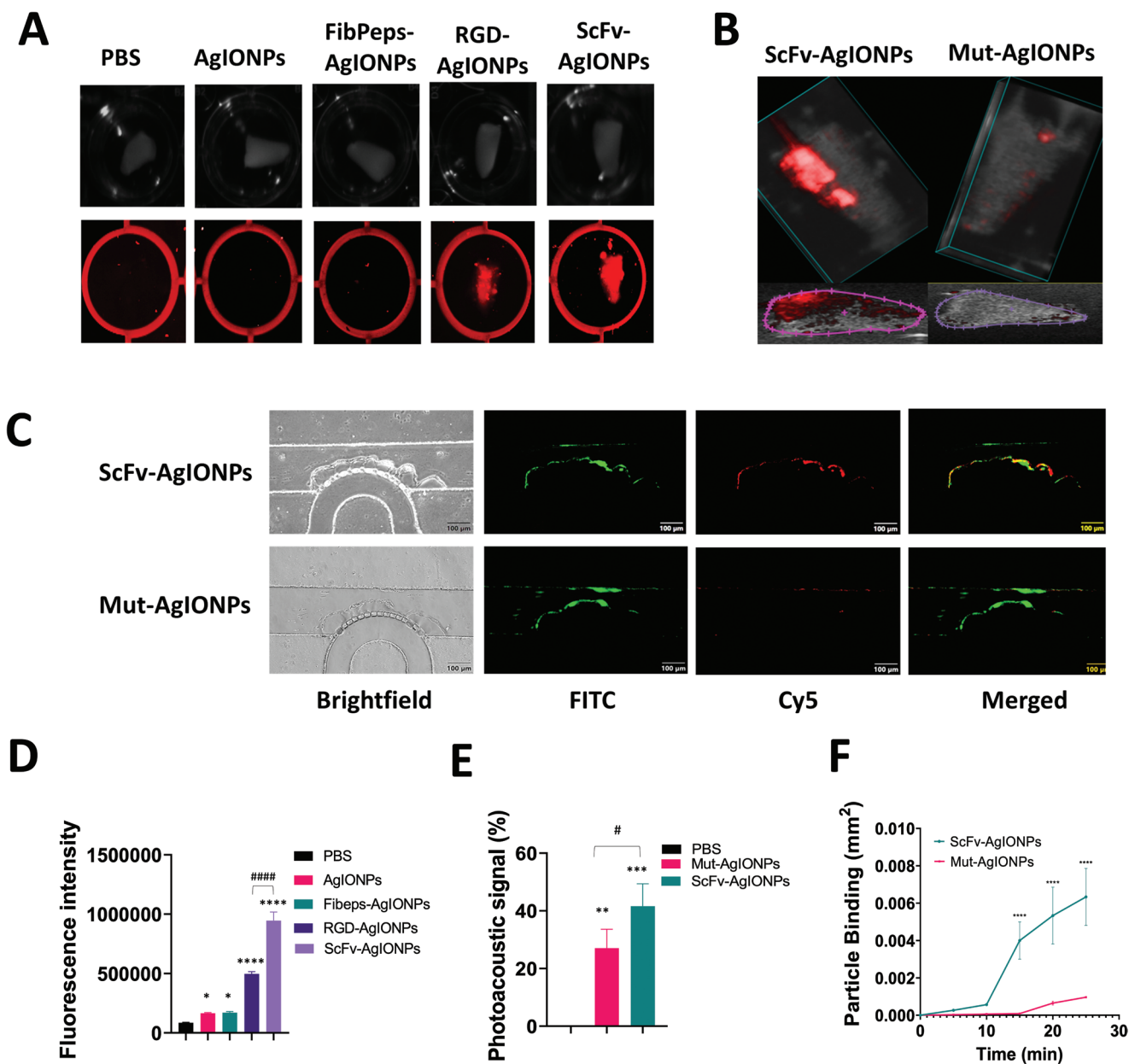NANO · MICRO
small
www.small-journal.com

Figure 3. Binding efficiency to in vitro human thrombi ($n = 3$). The concentration used for incubation of (A) and (B) was 0.1 mg mL^{-1} of the whole nanoparticle mass. For C, 0.5 mg mL^{-1}. A) Visible light images (grey) and fluorescence Sapphire images (red) taken after binding assay, and D) analysis from Fluorescence Sapphire images estimating binding to clot based on fluorescence intensity. B) PA images showing visible difference in photo acoustic signal (red) between the targeted nanoparticle when compared to the non-targeted nanoparticle with E) analysis showing significant difference between the binding of targeted and non-targeted nanoparticles. C,F) Images and graph of the flow binding assay, with scFv-AgIONPs (red fluorescence) illustrating higher binding to the DiOC6 stained platelets (green fluorescence) compared to mut-AgIONPs (scale bar = 100 μm). Sample size $n = 3$, $^{*}p < 0.05$ considered significant while $^{**}p < 0.01$, $^{***}p < 0.001$, and $^{****}p < 0.0001$, $^{\#}p < 0.05$, $^{\#\#\#\#}p < 0.0001$.

it shows no cytotoxicity in the viability studies performed. Endothelial cells treated with nanoparticles and laser showed a slight decrease in viability. Nevertheless, the viability was still ≈80% (Figure 4C). Tail bleeding assay confirmed no statistical difference in the bleeding times for the control and the treated mice, suggesting no risk of extreme bleeding caused by the treatment (Figure 4E). These data confirm the biocompatibility of the developed nanoparticles.

3.6. In Vivo Specific Binding of scFv-AgIONPs to Thrombus and Photothermal-Induced Thrombolysis

The specific binding of the nanoparticles was assessed in vivo using different imaging modalities, i.e., PAI and FI. Due to the small amount of iron in the AgIONPs, MRI was not feasible for imaging thrombosis in vivo. Nonetheless, AgIONPs should be further explored as a contrast agent for MRI in vivo using
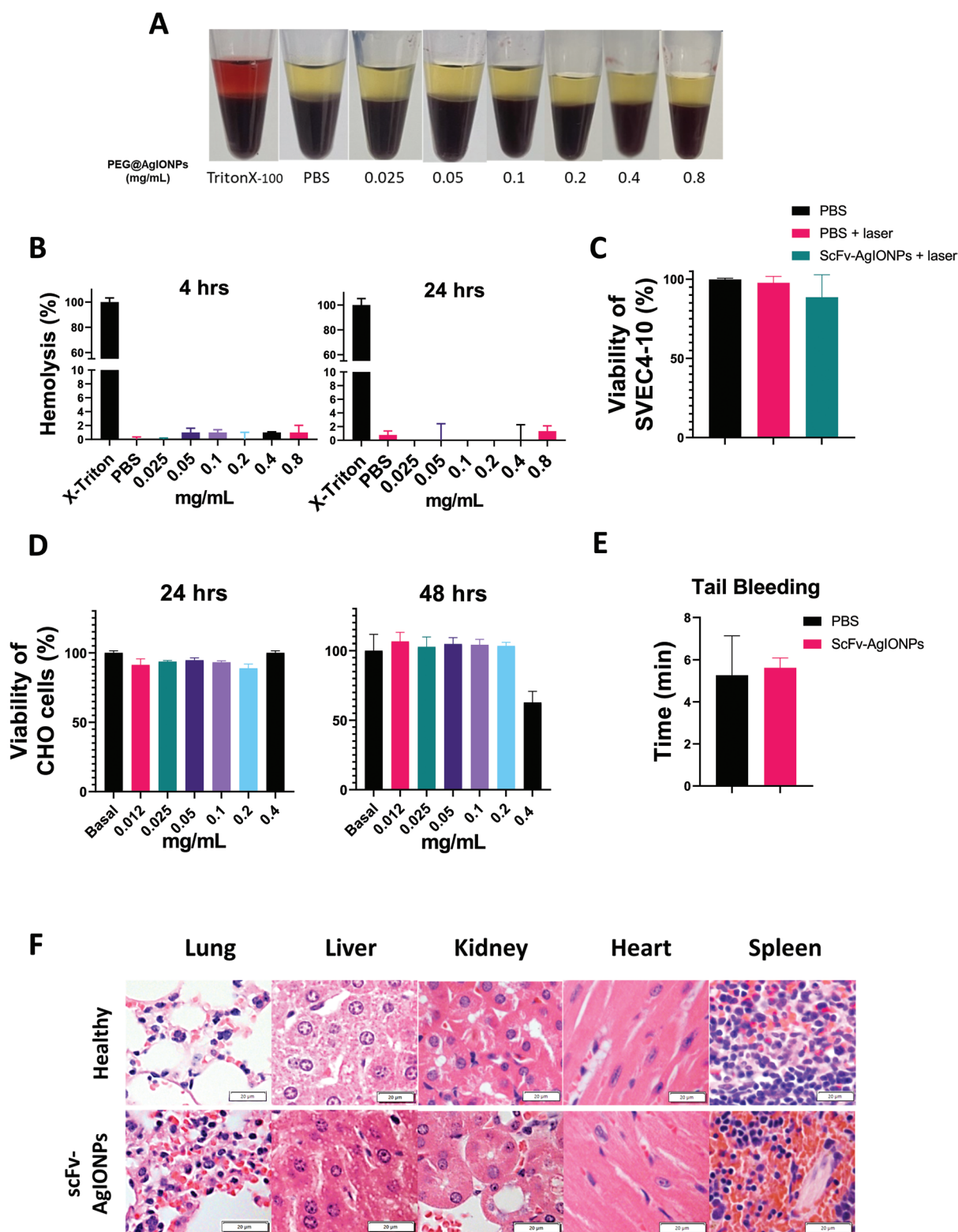
Figure 4. Biocompatibility of AgIONPs ($n = 3$). A) Eppendorf tubes with clear supernatant in the samples after 4 h incubated with PEG@AgIONPs and B) graphs showing hemolysis percentage after incubation with nanoparticles for 4 and 24 h suggesting no damage in red blood cells from the nanoparticles. C) Cytotoxicity of endothelial cells (SVEC4-10) after laser treatment with nanoparticles showing no decrease in viability. D) Cytotoxicity of PEG@AgIONPs to CHO cells after 1 and 2 days incubation. E) Graph showing no significant difference between the time taken for stopping the bleed between both groups, suggesting no risk of haemorrhages attributed to the treatment. F) Histology of tissues collected from healthy mice and mice treated with ScFv-AgIONPs and laser showing no apparent toxicity of the treatment (scale bar = 20 μm).

**ADVANCED
SCIENCE NEWS**

www.advancedsciencenews.com

NANO · MICRO

small

www.small-journal.com
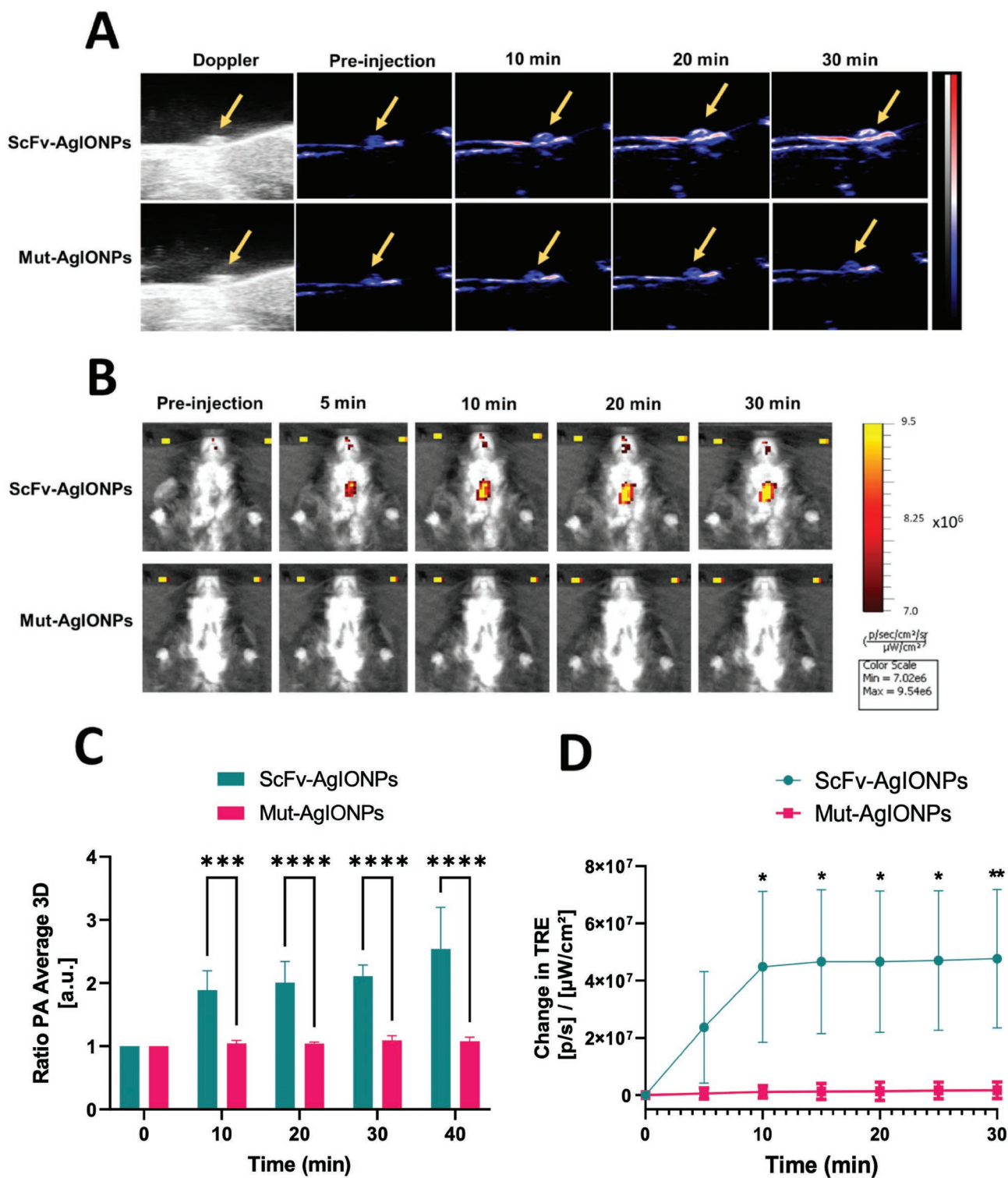
Figure 5. In vivo imaging. A) PAI images of thrombi (arrow pointing to the thrombosed artery) and B) FI images of mice treated with scFv-AgIONPs and mut-AgIONPs at different timepoints. C) PAI analysis graph showing statistical difference on the contrast signal since first timepoint and D) FI analysis graph of the relative total radiance efficiency in respect to baseline, showing statistical significance in the signal at 10 min (4 mg AgIONPs per kg of body weight, $n = 4$, $*p < 0.05$ considered significant while $**p < 0.01$, $***p < 0.001$, and $****p < 0.0001$).

other disease models where the region of interest has higher area such as cancer. PA imaging was performed before and after injection at different time points. **Figure 5**A shows the ultrasound and photoacoustic images before and after injection

ADVANCED
SCIENCE NEWS
www.advancedsciencenews.com

NANO · MICRO
small
www.small-journal.com

of photoacoustic signal. The images show a visual change in photoacoustic signal in the area treated with $AlCl_3$ and an increase in the strength of the signal over the time, suggesting that the targeted nanoparticles specifically and strongly attached to the thrombus. The ratio of the signal between scFv-AgIONPs and mut-AgIONPs doubled at 10 min, and it continued to increase over the time until it reached its peak at 40 min after injection (Figure 5C).

The fluorescence images were acquired before and every 5 min post-injection of the nanoparticles (Figure 5B). A relative increase in the total radiant efficiency (TRE) of the fluorescence was shown from 5 to 10 min post injection. Then the fluorescence remained stable and increased slowly for up to 30 min when compared to the pre-injection measurement. Notably, no increase in fluorescence was shown in the non-targeted group. These findings demonstrated the potential use of scFv-AgIONPs in providing a more specific, accurate, and sensitive multi-modality nanomaterial for detection of thrombosis.

The in vivo thrombolysis protocol used was optimized in the in vitro experiments using the same laser. Even though the in vitro optimization was done with a laser intensity of 1.5 W cm^{-2}, the carotid artery was damaged using this intensity (Figure S14, Supporting Information), and further optimization was needed. The optimal laser intensity in vivo was determined to be 1 W cm^{-2}. For evaluating the thrombolysis percentage, the blood flow before induction of clot, and before and after treatment was measured with a 0.5 mm flow probe (Figure S15, Supporting Information). **Figure 6** shows the data gathered from in vivo thrombolysis assay. A visual change between microscope images before and after laser treatment was observed for targeted nanoparticle groups (Figure 6A).

The changes in temperature after each cycle were neglectable between all groups except for the targeted. Importantly, there was no evidence of damage to the vessel nor the surrounding tissue after laser treatment even at the highest change in temperature. Figure 6B shows the quantitative data from the maximum and minimum value of the flow recorded by the flow probe. Blood restoration percentage was calculated by using the following formula, where F_0 is the basal normal flow, F_1 is the flow from the clotted artery before treatment, F_2 is the flow after treatment:

$$\text{Blood restoration (\%)} = \frac{(F_2 - F_1)(100)}{F_0} \qquad (1)$$

A full restoration of the blood flow was observed in the targeted group when compared to the control group. Mut-AgIONPs and free tPA groups had no difference between them nor the control group. Histology of carotid arteries stained with Masson's Trichrome showed similar data (Figure 6C). The remaining thrombus area (red) was significantly lower (<20%) for the groups treated with scFv-AgIONPs. Results from histology were also correlated with the restoration of flow and further confirmed there was no difference between the control, non-targeted and tPA groups. The dose of tPA used in this experiment was higher than the recommended dose of tPA used in the clinic (2 mg kg^{-1} versus 0.9 mg kg^{-1}).[80] Nevertheless, it is important to note that in the clinic, tPA must be administrated over 60–120 min, which will increase the circulation time of the thrombolytic.[81]

In addition, tPA is generally administered along with other therapeutics such as anticoagulants and repeat thrombolytic treatment is needed for complete resolution of symptoms.[82,83] Moreover, up to 25% of people still have a blood clot after thrombolytic therapy.[83] Altogether, this evidence can explain why in this study a single tail vein injection of free tPA at 2 mg kg^{-1} was not enough for causing thrombolysis. Surprisingly, our nanoparticles showed excellent photothermal thrombolysis alone. The mechanism of blood restoration in this study is known as hyperthermia-induced thrombolysis. Conversion of nonradiative light energy into heat is achieved by AgIONPs. Arterial thrombus is primarily composed of platelet aggregates in a reticulum of fibrin. When AgIONPs attach to the thrombus and are exposed by 808 nm laser, the generated hyperthermia will disrupt the fibrin matrix. In addition, heating of platelets and red blood cells will trigger apoptosis and eryptosis, respectively. The fibrinolysis and death cell caused by the AgIONPs heating will clear cellular material and protein from the compacted thrombi and will restore blood flow.[84] It is important to mention that the AgIONPs dose and settings of the laser treatment used in this study showed no effects on the viability of endothelial cells, suggesting that this nanosystem should not elicit adverse effects or harm to surrounding vasculature. Future studies should focus on the comparison between AgIONPs with tPA and tPA alone to explore a potential synergy for thrombolysis.

3.7. Biodistribution of PEG@AgIONPs

Vital organs were collected from the treated mice in order to track the biodistribution and estimate the biocompatibility of the nanoparticles to organs. The biodistribution was based on ex vivo fluorescence images, whereas the biocompatibility was microscopically observed from the morphology of the sectioned tissues. Based on the ex vivo images, most of the nanoparticles accumulated in the liver and kidneys (**Figure 7**A). Microscope images from histology tissues confirmed no acute abnormality detected in any of the analyzed tissues, including the liver and kidney (Figure 4F; Figure S16, Supporting Information). Ex vivo fluorescence imaging of carotid arteries suggests similar results as in vivo imaging, showing strong fluorescence on thrombi region for the targeted treated animals and a significant difference in the signal between the groups (Figure 7B). Importantly, there was no difference between the biodistribution of both groups.

4. Conclusion

We developed a novel nanoparticle system based on iron and silver to achieve simultaneous imaging and treatment of thrombosis. Following design, synthesis, and optimization, we demonstrated that our system shows promising theranostic utility through photoacoustic and fluorescence imaging, and laser-mediated photothermal thrombolysis in vivo and in vitro. The resulting AgIONPs were stable in PBS, had an asymmetrical shape, and strong absorbance in the NIR. AgIONPs specifically bond to thrombi in vitro and in vivo based on PAI and FI. Moreover, the nanoparticles served as an efficient photothermal agent to induce hyperthermia and showed excellent
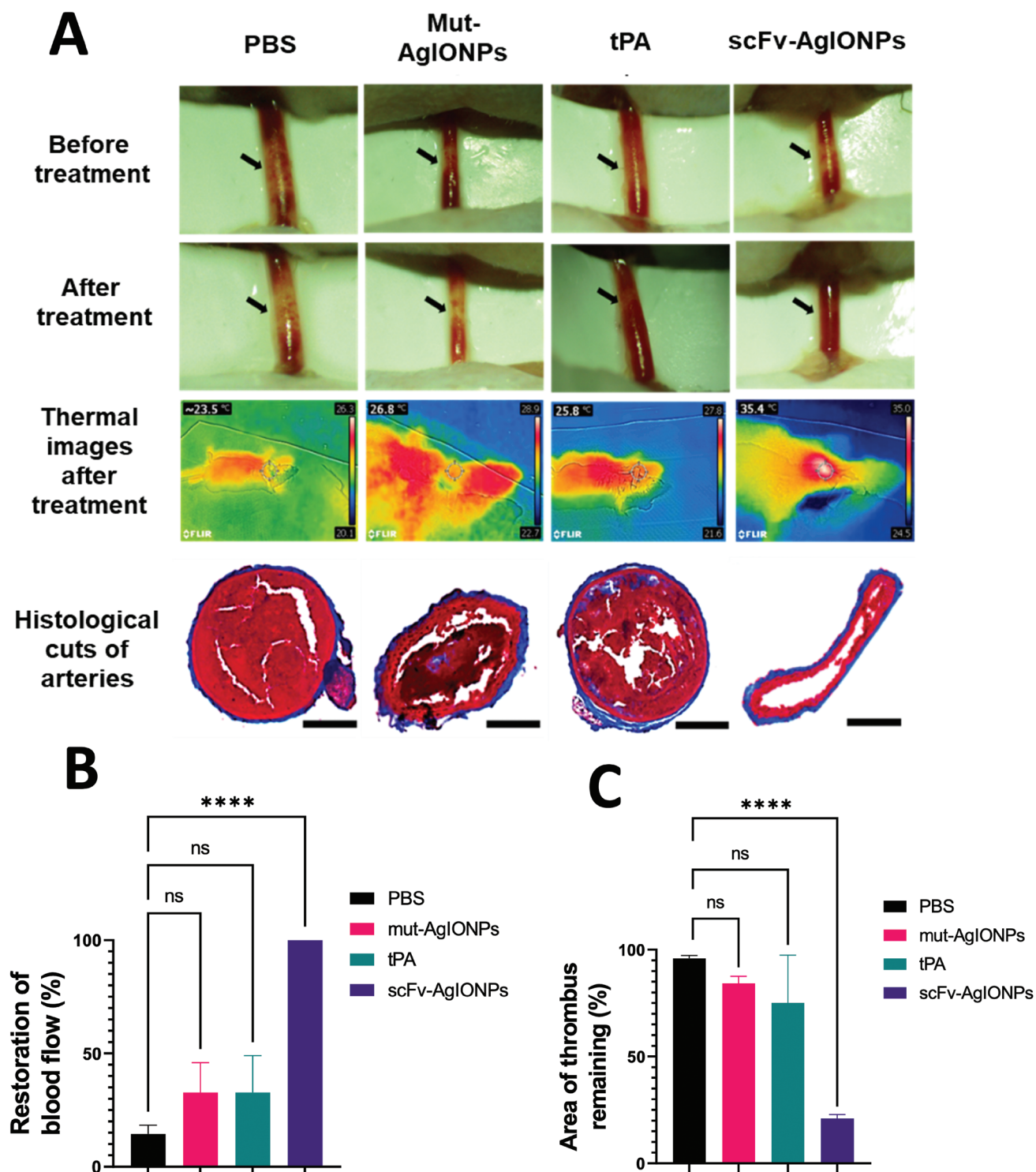
Figure 6. In vivo thrombolysis. AgIONPs were injected with a dose of 4 mg AgIONPs per kg of body weight and tPA groups were injected with 2 mg kg^{-1}. A) Images from the microscope showing arteries before and after treatment. Before treatment photos show the clot (arrow) in the arteries of all groups. After treatment photos suggest restoration of flow in targeted group, thrombolysis to some extent in tPA group and non-targeted group. Thermal photos show the increase in temperature from the last laser cycle of the treatment. Representative images of thrombosed arteries without or with thrombolytic therapy. Thrombus area appears red after staining with Masson's trichrome (scale bar = 100 μm). Thrombus area remaining in microscope images and histology show a significant reduction of the thrombus area group treated with scFv-AgIONPs ($n = 4$). B) Analysis from blood flow measurements showing significant differences between the groups treated with targeted nanoparticles and no significant differences between the non-targeted or free tPA groups. C) Graph from histology artery sections showing higher thrombus area in control, non-targeted and tPA groups. Data also shows almost complete thrombolysis for targeted group ($n = 4$, with $^*p < 0.05$ considered significant while $^{**}p < 0.01$, $^{***}p < 0.001$, and $^{****}p < 0.0001$).
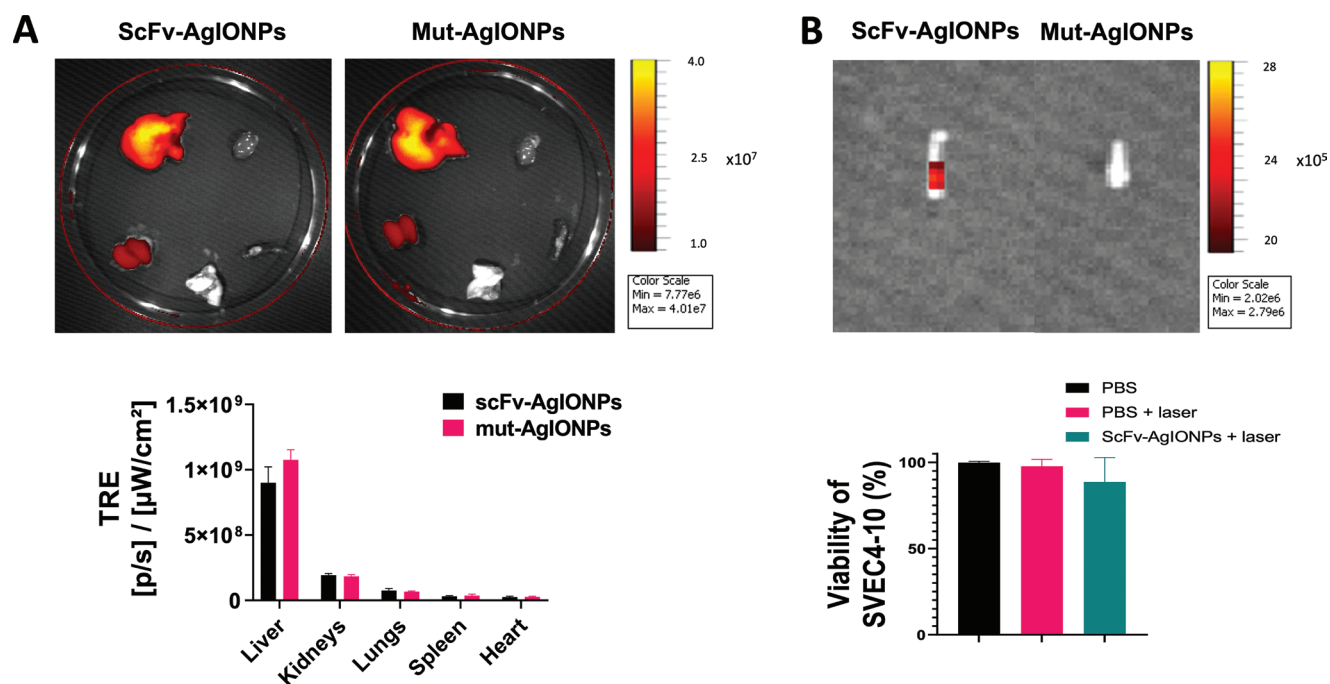
Figure 7. Ex vivo imaging. A) Fluorescence imaging tracking biodistribution of nanoparticles to vital organs and graph showing no difference between the targeted and non-targeted group. Ex vivo fluorescence shows that the nanoparticles are primarily distributed to the liver and kidneys. B) Ex vivo fluorescence imaging of carotids treated with targeted and non-targeted AgIONPs, showing a higher florescence in the thrombus area of the targeted group ($n = 4$, $^*p < 0.05$).

thrombolysis in vitro and complete blood flow restoration in vivo in a thrombosis mouse model. Hemocompatibility assays on red blood cells, viability assays on CHO and endothelial cells, and histology analysis suggested no apparent toxic effects of AgIONPs. Future studies should explore the possibility of using this nanosystem as a multimodal nanomaterial for treatment of thrombosis (i.e., loading of tPA and employing sono-thrombolysis). Altogether, we provide strong evidence that AgIONP is a promising non-invasive theranostic approach for imaging and treating thrombosis. This new class of silver nanoparticles could also be applied to other diseases such as cancer and infectious diseases.

Supporting Information

Supporting Information is available from the Wiley Online Library or from the author.

Conflict of Interest

The authors declare no conflict of interest.

Data Availability Statement

The data that support the findings of this study are available from the corresponding author upon reasonable request.

[1] WHO, *Cardiovascular diseases (CVDs)*, **2017**, https://www.who.int/health-topics/cardiovascular-diseases#tab=tab_1.

[2] ISTC, *World Thrombosis Day Empowers People Around the World to Recognize and Help Prevent Life-Threatening Blood Clots*, **2019**,

https://www.prnewswire.com/news-releases/world-thrombosis-day-empowers-people-around-the-world-to-recognize-and-help-prevent-life-threatening-blood-clots-300934190.html.

[3] A. Zia, Y. Wu, T. Nguyen, X. Wang, K. Peter, H. T. Ta, *Cardiovasc. Res.* **2020**, *116*, 2055.

[4] J. Palasubramaniam, X. Wang, K. Peter, *Arterioscler., Thromb., Vasc. Biol.* **2019**, *39*, e176.

[5] K. M. Woo, J. K. Goertz, *Emergency Medicine Practice* **2015**, *17*, 1.

[6] G. G. Gasparian, N. Sanossian, M. S. Shiroishi, D. S. Liebeskind, *J Stroke* **2015**, *10*, 298.

[7] O. Topaz, *Cardiovascular Thrombus: From Pathology and Clinical Presentations to Imaging, Pharmacotherapy and Interventions*, Academic Press, Asheville, NC **2018**.

[8] R. Corti, J. I. Osende, Z. A. Fayad, J. T. Fallon, V. Fuster, G. Mizsei, E. Dickstein, B. Drayer, J. J. Badimon, *J. Am. Coll. Cardiol.* **2002**, *39*, 1366.

[9] J. Silickas, S. A. Black, A. Phinikaridou, A. M. Gwozdz, A. Smith, P. Saha, *Methodist Debakey Cardiovasc. J.* **2018**, *14*, 188.

[10] F. C. Sampson, S. W. Goodacre, S. M. Thomas, E. J. R. Van Beek, *Eur. Radiol.* **2007**, *17*, 175.

[11] A. Y. Goktay, C. Senturk, in *Endovascular Treatment of Thrombosis and Embolism. Thrombosis and Embolism: from Research to Clinical Practice*, Springer, Berlin, Germany **2016**, pp. 195–213.

[12] R. S. Ramaswamy, S. Vedantham, *Endovascular Treatment of Deep Vein Thrombosis*, In: (Ed.: C. I. O. Chaar), Springer, Berlin, Germany **2018**, 331-341.

[13] N. Kucher, P. Boekstegers, O. J. Müller, C. Kupatt, J. Beyer-Westendorf, T. Heitzer, U. Tebbe, J. Horstkotte, R. Müller, E. Blessing, M. Greif, P. Lange, R.-T. Hoffmann, S. Werth, A. Barmeyer, D. Härtel, H. Grünwald, K. Empen, I. Baumgartner, *Circulation* **2014**, *129*, 479.

[14] M. G. Montiel Schneider, V. L. Lassalle, *Biomed. Pharmacother.* **2017**, *93*, 1098.

[15] Y. Liu, T. Hanley, H. Chen, S. R. Long, S. S. Gambhir, Z. Cheng, J. C. Wu, G. El Fakhri, B. Anvari, R. T. Zaman, *Sci. Rep.* **2020**, *10*, 5983.

[16] Y. Jin, C. Jia, S.-W. Huang, M. O'donnell, X. Gao, *Nat. Commun.* **2010**, *1*, 41.

[17] B. Du, C. Qu, K. Qian, Y. Ren, Y. Li, X. Cui, S. He, Y. Wu, T. Ko, R. Liu, X. Li, Y. Li, Z. Cheng, *Adv. Opt. Mater.* **2020**, *8*, 1901471.

[18] W. Xu, J. Leskinen, J. Tick, E. Happonen, T. Tarvainen, V.-P. Lehto, *ACS Appl. Mater. Interfaces* **2020**, *12*, 5456.

[19] G. Trujillo-De Santiago, M. J. Lobo-Zegers, S. L. Montes-Fonseca, Y. S. Zhang, M. M. Alvarez, *Microphysiol. Syst.* **2018**, *2*, 7.

[20] M. Chandarana, A. Curtis, C. Hoskins, *Appl. Nanosci.* **2018**, *8*, 1607.

[21] K. Vaidyanathan, S. Gopalakrishnan, *Cardiovasc. Hematol. Disord. Drug Targets* **2017**, *17*, 119.

[22] J. R. Mccarthy, *Nanomedicine* **2009**, *4*, 693.

[23] J. R. McCarthy, *Nanomed. Cardiovasc. Dis.* **2010**, *3*, 42.

[24] S. M. Dadfar, D. Camozzi, M. Darguzyte, K. Roemhild, P. Varvarà, J. Metselaar, S. Banala, M. Straub, N. Güvener, U. Engelmann, I. Slabu, M. Buhl, J. Van Leusen, P. Kögerler, B. Hermanns-Sachweh, V. Schulz, F. Kiessling, T. Lammers, *J. Nanobiotechnol.* **2020**, *18*, 22.

[25] E.-K. Lim, T. Kim, S. Paik, S. Haam, Y.-M. Huh, K. Lee, *Chem. Rev.* **2015**, *115*, 327.

[26] N. Dammes, D. Peer, *Theranostics* **2020**, *10*, 938.

[27] J. Tang, M. E. Lobatto, J. C. Read, A. J. Mieszawska, Z. A. Fayad, W. J. M. Mulder, *Curr. Cardiovasc. Imaging Rep.* **2012**, *5*, 19.

[28] Y. Wu, Y. Yang, W. Zhao, Z. P. Xu, P. J. Little, A. K. Whittaker, R. Zhang, H. T. Ta, *J. Mater. Chem. B* **2018**, *6*, 4937.

[29] J. R. Upponi, K. Jerajani, D. K. Nagesha, P. Kulkarni, S. Sridhar, C. Ferris, V. P. Torchilin, *Biomaterials* **2018**, *170*, 26.

[30] A. Ali, H. Zafar, M. Zia, I. Ul Haq, A. R. Phull, J. S. Ali, A. Hussain, *Nanotechnol. Sci. Appl.* **2016**, *9*, 49.

[31] R. Bhandari, P. Gupta, T. Dziubla, J. Z. Hilt, *Mater. Sci. Eng., C* **2016**, *67*, 59.

[32] S. Heid, H. Unterweger, R. Tietze, R. Friedrich, B. Weigel, I. Cicha, D. Eberbeck, A. Boccaccini, C. Alexiou, S. Lyer, *Int. J. Mol. Sci.* **2017**, *18*, 1837.

[33] Z. Surowiec, M. Budzyński, K. Durak, G. Czernel, *Nukleonika* **2017**, *62*, 73.

[34] H. T. Ta, N. Arndt, Y. Wu, H. J. Lim, S. Landeen, R. Zhang, D. Kamato, P. J. Little, A. K. Whittaker, Z. P. Xu, *Nanoscale* **2018**, *10*, 15103.

[35] H. T. Ta, Z. Li, C. E. Hagemeyer, G. Cowin, S. Zhang, J. Palasubramaniam, K. Alt, X. Wang, K. Peter, A. K. Whittaker, *Biomaterials* **2017**, *134*, 31.

[36] H. Ta, Z. Li, C. Hagemeyer, G. Cowin, J. Palasubramaniam, K. Peter, A. Whittaker, *Atherosclerosis* **2017**, *263*, e146.

[37] A. Saraswathy, S. S. Nazeer, M. Jeevan, N. Nimi, S. Arumugam, V. S. Harikrishnan, P. R. H. Varma, R. S. Jayasree, *Colloids and Surfaces B, Biointerfaces* **2014**, *117*, 216.

[38] L. Mohammed, H. G. Gomaa, D. Ragab, J. Zhu, *Particuology* **2017**, *30*, 1.

[39] M. K. Gupta, Y. Lee, T. C. Boire, J.-B. Lee, W. S. Kim, H.-J. Sung, *Nanotheranostics* **2017**, *1*, 166.

[40] C. Chouly, D. Pouliquen, I. Lucet, J. J. Jeune, P. Jallet, *J. Microencapsulation* **1996**, *13*, 245.

[41] A. Hatef, B. Darvish, A. Dagallier, Y. R. Davletshin, W. Johnston, J. C. Kumaradas, D. Rioux, M. Meunier, *J. Phys. Chem. C* **2015**, *119*, 24075.

[42] O. Veiseh, J. W. Gunn, M. Zhang, *Adv. Drug Delivery Rev.* **2010**, *62*, 284.

[43] M.-F. Tsai, C. Hsu, C.-S. Yeh, Y.-J. Hsiao, C.-H. Su, L.-F. Wang, *ACS Appl. Mater. Interfaces* **2018**, *10*, 1508.

[44] L. L. Ma, M. D. Feldman, J. M. Tam, A. S. Paranjape, K. K. Cheruku, T. A. Larson, J. O. Tam, D. R. Ingram, V. Paramita, J. W. Villard, J. T. Jenkins, T. Wang, G. D. Clarke, R. Asmis, K. Sokolov, B. Chandrasekar, T. E. Milner, K. P. Johnston, *ACS Nano* **2009**, *3*, 2686.

[45] A. U. Rehman, Y. Wu, H. D. N. Tran, K. Vazquez-Prada, Y. Liu, H. Adelnia, N. D. Kurniawan, M. N. Anjum, S. S. Moonshi, H. T. Ta, *ACS Appl. Nano Mater.* **2021**, *4*, 10136.

[46] H. Ammari, Y. Deng, P. Millien, *Arch. Ration. Mech. Anal.* **2016**, *220*, 109.

[47] G. Baffou, R. Quidant, *Laser Photon. Rev.* **2013**, *7*, 171.

[48] V. Amendola, R. Pilot, M. Frasconi, O. M. Marago, M. A. Iati, *J. Phys.: Condens. Matter* **2017**, *29*, 203002.

[49] M. A. Mackey, M. R. K. Ali, L. A. Austin, R. D. Near, M. A. El-Sayed, *J. Phys. Chem. B* **2014**, *118*, 1319.

[50] F. Liu, S.-y. Du, *Sci. Rep.* **2020**, *10*, 1.

[51] D. R. Raj, S. Prasanth, T. Vineeshkumar, C. Sudarsanakumar, *Sens. Actuators, B* **2016**, *224*, 600.

[52] D. D. Evanoff Jr, G. Chumanov, *ChemPhysChem* **2005**, *6*, 1221.

[53] W. Li, X. Chen, *Nanomedicine* **2015**, *10*, 299.

[54] K. A. Homan, M. Souza, R. Truby, G. P. Luke, C. Green, E. Vreeland, S. Emelianov, *ACS Nano* **2012**, *6*, 641.

[55] K. Pu, A. J. Shuhendler, J. V. Jokerst, J. Mei, S. S. Gambhir, Z. Bao, J. Rao, *Nat. Nanotechnol.* **2014**, *9*, 233.

[56] Z. Chaudhary, G. M. Khan, M. M. Abeer, N. Pujara, B. Wan-Chi Tse, M. A. Mcguckin, A. Popat, T. Kumeria, *Biomater. Sci.* **2019**, *7*, 5002.

[57] F. Akther, J. Zhang, H. D. N. Tran, H. Fallahi, H. Adelnia, H.-P. Phan, N.-T. Nguyen, H. T. Ta, *Adv. Biol.* **2022**, *6*, 2101316.

[58] J. Viereck, F. L. Ruberg, Y. Qiao, A. S. Perez, K. Detwiller, M. Johnstone, J. A. Hamilton, *Arterioscler., Thromb., Vasc. Biol.* **2005**, *25*, 240.

[59] O. Ivashchenko, M. Lewandowski, B. Peplińska, M. Jarek, G. Nowaczyk, M. Wiesner, K. Załęski, T. Babutina, A. Warowicka, S. Jurga, *Mater. Sci. Eng., C* **2015**, *55*, 343.

ADVANCED
SCIENCE NEWS

www.advancedsciencenews.com

NANO · MICRO
small
www.small-journal.com

[60] N. R. Jana, L. Gearheart, C. J. Murphy, *Langmuir* **2001**, *17*, 6782.

[61] N. Zhu, H. Ji, P. Yu, J. Niu, M. Farooq, M. Akram, I. Udego, H. Li, X. Niu, *Nanomaterials* **2018**, *8*, 810.

[62] X. Zhou, X. Huang, X. Qi, S. Wu, C. Xue, F. Y. C. Boey, Q. Yan, P. Chen, H. Zhang, *J. Phys. Chem. C* **2009**, *113*, 10842.

[63] S. Dunn, S. Sharp, S. Burgess, *Nanotechnology* **2009**, *20*, 115604.

[64] M. V. Cañamares, J. V. Garcia-Ramos, J. D. Gómez-Varga, C. Domingo, S. Sanchez-Cortes, *Langmuir* **2005**, *21*, 8546.

[65] T. T. Hien Pham, C. Cao, S. J. Sim, *J. Magn. Magn. Mater.* **2008**, *320*, 2049.

[66] Materials Evaluation and Engineering I, *Energy Dispersive X-ray Spectroscopy (EDS)*, **2020**, https://www.mee-inc.com/laboratory-expertise/energy-dispersive-x-ray-spectroscopy-eds/.

[67] D. Paramelle, A. Sadovoy, S. Gorelik, P. Free, J. Hobley, D. G. Fernig, *Analyst* **2014**, *139*, 4855.

[68] G. Fu, W. Liu, S. Feng, X. Yue, *Chem. Commun.* **2012**, *48*, 11567.

[69] J.-W. Xiao, S.-X. Fan, F. Wang, L.-D. Sun, X.-Y. Zheng, C.-H. Yan, *Nanoscale* **2014**, *6*, 4345.

[70] J. Zhou, Z. Lu, X. Zhu, X. Wang, Y. Liao, Z. Ma, F. Li, *Biomaterials* **2013**, *34*, 9584.

[71] X. Liu, B. Li, F. Fu, K. Xu, R. Zou, Q. Wang, B. Zhang, Z. Chen, J. Hu, *Dalton Trans.* **2014**, *43*, 11709.

[72] Q. Tian, F. Jiang, R. Zou, Q. Liu, Z. Chen, M. Zhu, S. Yang, J. Wang, J. Wang, J. Hu, *ACS Nano* **2011**, *5*, 9761.

[73] Q. Hu, K. Wang, L. Qiu, *Colloids Surf., B* **2021**, *197*, 111372.

[74] K. X. Vazquez-Prada, J. Lam, D. Kamato, Z. P. Xu, P. J. Little, H. T. Ta, *Arterioscler., Thromb., Vasc. Biol.* **2021**, *41*, 601.

[75] L. Liu, C. A. Burnyeat, R. S. Lepsenyi, I. O. Nwabuko, T. L. Kelly, *Chem. Mater.* **2013**, *25*, 4206.

[76] H. T. Ta, S. Prabhu, E. Leitner, F. Jia, D. Von Elverfeldt, K. E. Jackson, T. Heidt, A. K. N. Nair, H. Pearce, C. Von Zur Muhlen, X. Wang, K. Peter, C. E. Hagemeyer, *Circ. Res.* **2011**, *109*, 365.

[77] M. V. A. van Moorsel, R. T. Urbanus, S. Verhoef, C. A. Koekman, M. Vink, T. Vermonden, C. Maas, G. Pasterkamp, R. M. Schiffelers, *Int. J. Pharm. X* **2019**, *1*, 100020.

[78] H. T. Ta, N. P. Truong, A. K. Whittaker, T. P. Davis, K. Peter, *Expert Opin. Drug Deliv.* **2018**, *15*, 33.

[79] N. Trier, P. Hansen, G. Houen, *Int. J. Mol. Sci.* **2019**, *20*, 6289.

[80] Genentech USA I, *Dosing & Administration of Activase*, **2016**, https://www.genentechmaterials.com/activase/items.sgi.

[81] Medscape, *Alteplase*, **2022**, https://reference.medscape.com/drug/activase-tpa-alteplase-342287.

[82] A. Vanood, S. Santhakumar, A. Said, *Interdisciplinary Neurosurgery* **2021**, *23*, 100937.

[83] *Cleveland Clinic, Thrombolytic Therapy*, **2022**, https://my.clevelandclinic.org/health/treatments/23345-thrombolytic-therapy.

[84] D. Cabrera, M. E. Sharifabad, J. A. Ranjbar, N. D. Telling, A. G. S. Harper, *J. Thromb. Haemostasis* **2022**, *20*, 2556.

2205744 (16 of 16)